Coherent Diffractive Imaging with Diffractive Optics

Jakob Soltau,[1,*] Markus Osterhoff,[1,2] and Tim Salditt[1,2,†]
[1]*Institut für Röntgenphysik, Georg-August-Universität Göttingen, Friedrich-Hund-Platz 1, Göttingen 37077, Germany*
[2]*Campus-Institut Data Science, Friedrich-Hund-Platz 1, Göttingen 37077, Germany*

(Received 10 December 2021; revised 14 March 2022; accepted 15 April 2022; published 31 May 2022)

We present a novel approach to x-ray microscopy based on a multilayer zone plate which is positioned behind a sample similar to an objective lens. However, unlike transmission x-ray microscopy, we do not content ourselves with a sharp intensity image; instead, we incorporate the multilayer zone plate transfer function directly in an iterative phase retrieval scheme to exploit the large diffraction angles of the small layers. The presence of multiple diffraction orders, which is conventionally a nuisance, now comes as an advantage for the reconstruction and photon efficiency. In a first experiment, we achieve sub-10-nm resolution and a quantitative phase contrast.

DOI: 10.1103/PhysRevLett.128.223901

X-ray microscopy enables imaging of matter at high resolution down to the 10 nm range [1–5], with chemical sensitivity [6] and at ultrafast timescales [7–9]. Above all, it offers unique advantages for nondestructive imaging of bulk and optically intransparent samples. For biological matter and complex nanomaterials, full-field imaging is particularly suitable, since it can cover large specimens without the need for scanning. Conceptually, there are three very different approaches to full-field x-ray microscopy. The first modern x-ray microscopes, so-called transmission x-ray microscopes (TXMs), were developed in the 1970s. They used Fresnel zone plates (FZPs) as objective lenses to directly image and magnify the sample structure, relying on a sharp image in the detection plane [10]. To circumvent the problems associated with low diffraction efficiencies and imperfect FZP lenses, coherent diffractive imaging (CDI) was introduced [11,12], replacing lens-based image formation by an iterative phase retrieval algorithm, to invert a coherent diffraction pattern of a compact sample. For extended samples, the ptychographic variant of CDI proved particularly well suited [13], which solves the phase problem based on partial overlap between subsequent acquisitions using a finite beam. Despite impressive progress in dose efficiency and fast scanning [14], overhead due to motor movement still imposes constraints on the scan time and limits the observation of fast dynamic processes. Furthermore, scanning is incompatible with single pulse imaging at free-electron lasers (FELs). The third full-field x-ray microscopy approach, finally, is based on inline holography in a cone-beam geometry [5,15–17]. Because of its adjustable field-of-view (FOV) and resolution, and comparatively well-posed phase problem, it performs very well for tomography of weakly contrasted biological samples [18,19].

Notwithstanding the advantages of the more recent lensless approaches to microscopy, it is timely to revisit lens-based x-ray microscopy. Since CDI was proposed 20 years ago, significant progress in nanofabrication has resulted in high resolution and high efficiency zone plate optics, in particular, multilayer zone plates (MZPs) and one-dimensional multilayer Laue lenses (MLLs), which can focus an x-ray beam to a size of sub-10-nm (full width at half maximum, FWHM) [20–22]. Unfortunately, however, this focusing capability does not directly translate to an equivalent resolution in full-field imaging, due to a number of complications associated with multiple diffraction orders, volume diffraction, remaining aberrations, and the need of Zernike phase rings for phase contrast. At the same time, the recently achieved 10 nm resolution in absorption contrast shows the potential of high resolution zone plate optics [4].

In this Letter, we present a novel approach to full-field hard x-ray microscopy, combining conceptional aspects of all three major developments and their corresponding advantages. The proposed method is, in particular, applicable to high brilliance synchrotron sources and uniquely suited to implement high resolution single pulse imaging at FELs. We use a MZP as an objective lens to achieve high resolution but do not content ourselves with a sharp intensity image; instead, we use a fully quantitative and iterative phase retrieval scheme to reconstruct the sample transmission function. To this end, we use the measured MZP transfer function. This liberates us from the requirement to use perfectly aligned, aberration- and distortion-free optics, and allows us to exploit the full information and numerical aperture (NA) of the diffraction pattern with the sample encoded in near- and far-field intensity

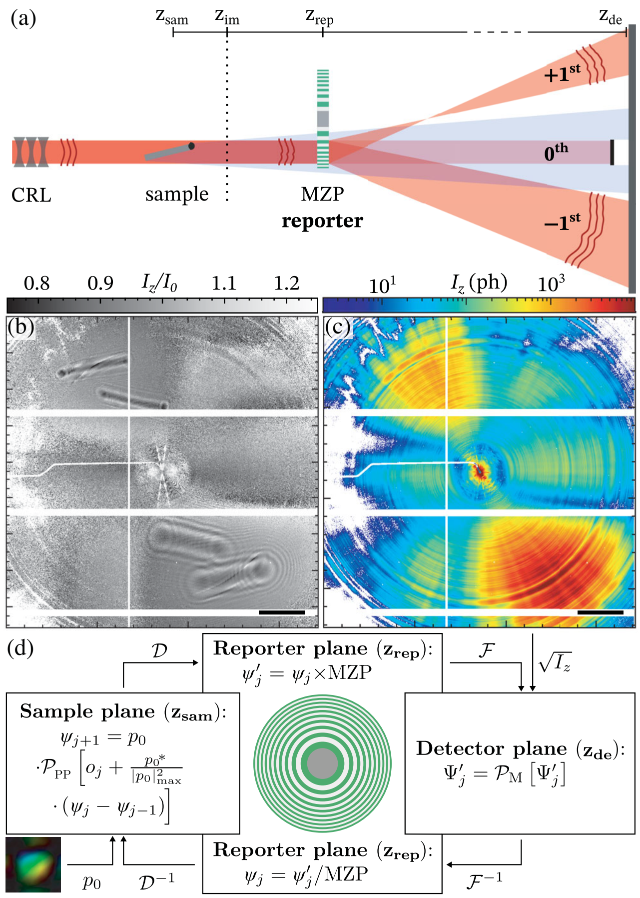

FIG. 1. (a) Schematic of the RBI setup. A coherent x-ray beam (red) is focused by CRLs onto the sample, here a nanowire (NW), and a MZP is positioned as a reporter in the near field. The MZP diffracts the beam into the −first, +first, and zeroth diffraction order recorded in the far field. The blue color indicates the CDI diffraction signal of the sample. (b) The empty divided detector image indicating the three different sample (NW) signals (two holograms and one CDI signal) recorded in a single measurement (linear gray scale). (c) The intensity measurement with the sample (NW) in the beam. This single measurement is used for the sample reconstruction. The acquisition time was 5 s (logarithmic color scale). (d) Outline of the RBI algorithm. $\mathcal{D}$, $\mathcal{D}^{-1}$ denotes the near- and $\mathcal{F}$, $\mathcal{F}^{-1}$ far-field propagators, $\mathcal{P}_{\mathrm{PP}}$ the pure phase and $\mathcal{P}_{\mathrm{M}}$ the magnitude constraint, p_0 the incident illumination function, and MZP the transfer function of the MZP. Scale bars: 250 pixels corresponding to a scattering vector $q = 0.15\ \mathrm{nm}^{-1}$.

distributions. Using this scheme, we experimentally demonstrate sub-10-nm resolution and quantitative contrast of the measured sample. We refer to the imaging scheme as reporter-based imaging (RBI), because in contrast to the conventional application of an objective lens to acquire a sharp image of the sample, we use the MZP as a reporter of the near field behind the sample, rather than trying to obtain a sharp image in the detector plane.

Figure 1 illustrates the RBI scheme demonstrated experimentally at the GINIX instrument [23] of the coherence beamline P10 of the PETRA III storage ring (Hamburg, Germany). In Fig. 1(a), the basic optical concept of RBI is shown, with the sample in plane z_{sam} illuminated by a coherent microfocus, with low divergence and a spot size defining the FOV. The reporter structure, here composed of a MZP with focal length f, is positioned behind the sample in plane z_{rep}. The MZP diffracts the incident beam, mostly to the zeroth, +first, and −first order. The zeroth order corresponds to a conventional CDI signal (without MZP). All signals are acquired by the same detector positioned in the far field at z_{de}. Figures 1(b) and 1(c) show typical full-field diffraction images of the sample corresponding to the same exposure Fig. 1(b) with and Fig. 1(c) without empty beam division. With $|z_{\mathrm{de}} - z_{\mathrm{rep}}| \gg f$, the image plane of the MZP (z_{im}) is close to its focal plane. The distance of the sample to the image plane ($|z_{\mathrm{im}} - z_{\mathrm{sam}}|$) defines the defocus distance for the coherent imaging scheme. In other words, the MZP images the defocus plane onto the detector. This is visible in the empty beam divided detector image shown in Fig. 1(b). Two magnified near-field intensity distributions (inline holograms) are recorded in different areas on the detector at different effective defocus distances corresponding to the +first (upper left corner) and −first (lower right corner) MZP diffraction order. The spatial separation of these signals on the detector is controlled by the off-axis translation of the MZP, as illustrated in Fig. 1(a). In Fig. 1(c), showing the undivided detector image (I_z) on a logarithmic scale (acquisition time 5 s), the diffraction of the incident beam in the +first and −first order can be distinguished based on the corresponding high-flux areas (color code red). The concentric rings around the center are imprints of the zones of the MZP. Altogether, the detector records three different but complementary signals of the sample in a single intensity measurement: a conventional CDI signal visible around the center, and in addition, holograms of the sample encoded in the divergent beams of the +first and −first MZP diffraction orders. The data were acquired at the following configuration and parameters: The undulator beam was monochromatized by a Si(111) channel-cut monochromator to a photon energy of 8 keV and focused by beryllium CRLs with a divergence of 0.05 mrad to a spot size of $3.0 \times 3.7\ \mu\mathrm{m}^2$ (FWHM) defining the FOV. The sample consisted of InP nanowires (NWs) with a diameter of 200 nm and a length of 2.8 μm, terminated by an Au tip at one end, and was deposited on an Si_3N_4 window. The distance between the sample z_{sam} and the MZP z_{rep} was 878 μm. The position of the sample was chosen to be close but not equal to the imaging plane z_{im}. A more detailed discussion on the position z_{sam} can be found in the numerical simulations of Ref. [24]. The MZP was composed of 784 zones, an outermost zone width of 5 nm, and a focal length of 530 μm [25]. The diameter of the MZP was 16.9 μm with an optical depth of 1.2 μm. The focus of a similar MZP was characterized by ptychography in Ref. [22]. The MZP was also mounted on an Si_3N_4

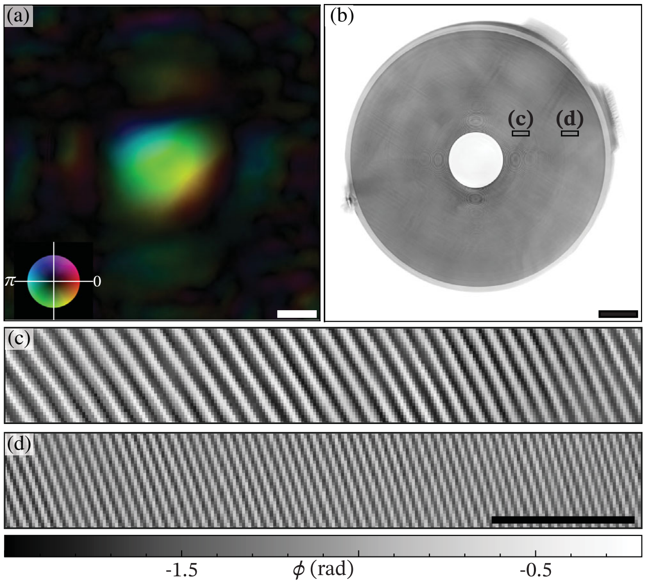

FIG. 2. (a) Ptychographic reconstruction of (a) the probe amplitude and phase at z_{rep} with a FWHM of the intensity profile of $3.0 \times 3.7\ \mu\mathrm{m}^2$ and (b) the MZP. The enlargements (c), (d) show the radially decreasing zone widths. Scale bars: (a),(b) 2.5 μm; (c),(d) 250 nm.

window. The coherent diffraction patterns were recorded with a single photon counting pixel detector (Eiger 4M, Dectris Ltd. Switzerland) positioned at a distance of 5.05 m behind the MZP, with 2167×2070 pixels and a pixel size of 75 μm.

Figure 1(d) outlines the iterative RBI phase retrieval algorithm operating on a single intensity measurement I_z of the sample, such as the one shown in Fig. 1(c). In addition to the input $\sqrt{I_z}$, the probe function illuminating the sample p_0 and the transfer function of the MZP were used. p_0 and the structure of the MZP were reconstructed by a prior ptychographic scan without sample (see Fig. 2). RBI is based on the propagation of the wave field ψ_j between the sample plane z_{sam} and the detector plane z_{de}. But unlike conventional approaches, the propagation is performed not in a single step using a near- or far-field propagator but in three substeps: (i) near-field propagation ($\mathcal{D}$) from z_{sam} to z_{rep} ($\psi_j = \mathcal{D}[\psi_j]$), (ii) multiplication of the reporter transfer function ($\psi'_j = \psi_j \times \mathrm{MZP}$), and (iii) far-field propagation ($\mathcal{F}$) to z_{de} ($\Psi'_j = \mathcal{F}[\psi'_j]$). The three-step approach with applied knowledge in each field builds upon the seminal work [26] to reconstruct a divergent wave field and Ref. [27] for imaging. In both cases, it has been shown that the use of multiple planes in a single-shot approach is beneficial for phase retrieval. As usual, compatibility with the measured data is assured in z_{de} by applying the magnitude constraint: $\mathcal{P}_M[\Psi'_j] = \sqrt{I_z} \times \Psi'_j/|\Psi'_j|$. The updated wave field (Ψ'_j) is backpropagated using the inverse operations: (iii) $\psi'_j = \mathcal{F}^{-1}[\Psi'_j]$, (ii) $\psi_j = \psi'_j/\mathrm{MZP}$, and (i) $\psi_j = \mathcal{D}^{-1}[\psi_j]$. In z_{sam}, the object o_j and probe function p are separated. The separation and the update of o_j is performed equivalent to the standard extended ptychographic update function (ePIE) [28] as written in Fig. 1(d), in combination with a pure phase constraint P_{PP}, well justified for hard x-ray imaging of nanomaterials such as NWs. The P_{PP} acts on o_j as $\mathcal{P}_{\mathrm{PP}}[o_j] = \exp[i\phi(o_j)]$. Alternatively, depending on the specific imaging problem, other object projectors could be implemented such as range, support, shearlet (sparsity), or homogeneous object constraints [29]. The updated object (o_{j+1}) is multiplied with the initial (not updated) probe function p_0 to generate the updated wave field ψ_{j+1} for the next iteration. Besides the ePIE update scheme of the wave field, different approaches could be used such as alternating projections (AP) [30] or the relaxed averaged alternating reflector (RAAR) [31]. But importantly, for the reconstruction of the object, the transfer function of the MZP and the probe illumination function have to be known. Both were obtained by ptychography before the single frame acquisition of the sample.

In Fig. 2(a) the reconstructed probe and Fig. 2(b) the phase of the reconstructed MZP are shown. The enlarged regions in Figs. 2(c) and 2(d) show the radially decreasing zone widths of the MZP. The pixel size of the reconstruction is 5.2 nm. The probe illumination function in Fig. 2(a) shows a nearly flat phase in the maximum and side maxima of only low intensity. For the reconstruction, two ptychographic scans (without the NWs) were recorded with 41×41 scan positions, one with a beamstop and high photon flux and one without but with a photon flux reduced by attenuators. The acquisition time per point was 3 and 1 s for the scan without and with beamstop, respectively. A customized ptychographic code based on the ePIE update approach [28] was used. Both scans were used for the reconstruction of the probe and the object in a combined scheme, alternating between the wave field update using the detector image without and with the beamstop. This approach was chosen since the center beam contains primarily information of the probe, whereas the different diffraction orders of the MZP are recorded with a much higher signal-to-noise ratio using no attenuators (with a beamstop).

Figure 3(a) shows the RBI reconstruction of the NWs. Both NWs are resolved, including the Au tip at the end of each wire. The blue circle indicates the area where the intensity of the incident illumination falls below 10% of the maximum intensity. This results in a lower contrast, as can be seen by the Au tip of the left NW. One-hundred iterations were already sufficient for the reconstruction. Given the redundancy by the three diffraction signals, no artifacts of detector gaps appear in the reconstruction. The enlargement of the tip of the NW on the right side is presented in Fig. 3(b). The round Au tip and the InP main part are resolved. Below the transition from the Au tip to the NW main part, a small change in contrast is visible,

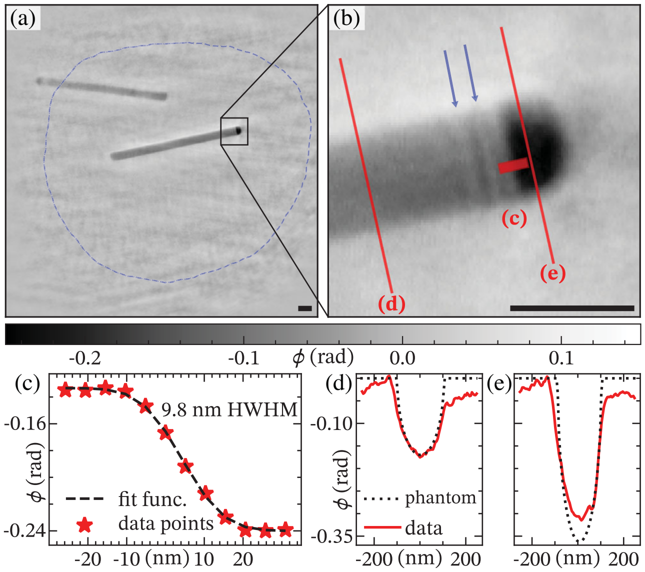

FIG. 3. (a) Reconstructed NWs using RBI using the detector image shown in Fig. 1(d). The NWs have a 200 nm diameter and an Au tip at one end. The blue circle indicates the area where the relative intensity is below 10%. (b) Enlarged region of one NW tip. (c) Error fit of the material edge indicated in (b), resulting in a resolution (half-period) of 9.8 nm. (d) Line profile of the InP main part of the NW and (e) of the Au tip compared with expected phase shifts of a NW phantom. Scale bars: 250 nm.

resembling rings around the NW (indicated by two blue arrows). With the current measurements, it is very plausible that theses fringes are not a reconstruction artifact but an effect of structural defects within the wires associated with rotational twinning. The observed rings are similar in appearance to scanning and transmission electron microscopy of similar InP NWs [32]. It should be noted that rotational twinning does not change the electron density, only the crystal structure. Although in coherent diffractive imaging the differences in the phase shift are attributed to a difference in the electron density, the diffraction of photons by small features beyond the NA of the detector could result in small variations in the reconstruction. The resolution of the phase image is determined by an edge fit. Since the NWs are cylindrically shaped objects, the steepest edge of the NW is the transition of the Au tip to the InP main part. The red rectangle in Fig. 3(b) indicates the region of the edge fit. The result is shown in Fig. 3(c) indicating a steepness (half-width at half maximum, HWHM) and thus a resolution of 9.8 nm. In Figs. 3(d) and 3(e), the phase shift of the reconstructed NW is compared to the phase shift of a phantom model using the NW design parameters to demonstrate that the phase shift reconstructed by RBI is in quantitative agreement with expectation, up to only a small deviation for the NW Au tip.

Next we discuss the RBI scheme, first in comparison to conventional CDI, then to TXM, and finally to inline holography. In comparison to CDI, RBI has the following advantages: (I) Given the strong signals of the MZP diffraction orders, the possible resolution is enhanced with respect to the CDI signal without the MZP, which would be limited to a smaller NA for weakly scattering samples. (II) The low and moderate spatial frequencies are encoded not only in a few center pixels but are distributed over large detector areas due to the magnification by the MZP diffraction orders. The fact that the diffraction pattern is not centrosymmetric (broken Friedel symmetry) results in an enhanced "diversity" and allows the reconstruction of extended samples without the necessity of a support mask. Additionally, at least three different images of the sample structure are encoded in a single diffraction pattern, the +first and −first MZP diffraction orders and the CDI signal. This gives a strong redundancy which can be exploited for the reconstruction and can compensate missing information due to intermodular gaps and a beamstop. In contrast to coherent modulation imaging [33], here we redefine the purpose of the modulator by exploiting the magnifying capabilities of the MZP given its outermost zone width of 5 nm, as we had already suggested in Refs. [24,34]. Thereby, we additionally relax the sampling constraint and achieve a high magnification of the sample. A comparison between a sample reconstructed with RBI and reconstructed with conventional CDI, in equal configurations is shown in the Supplemental Material [35]. Notwithstanding the mentioned advantages of a reporter structure, it must be noted that the corresponding absorption (in the reporter) decreases the dose efficiency. By using a MZP with an optical depth of only 1.2 μm corresponding to an absorption of 13.1%, we keep this effect at a tolerable level.

In comparison to conventional (incoherent) TXM, RBI has the following advantages: (i) The reconstruction from a single detector image is not limited to either phase or absorption contrast, and (ii) the reconstructed sample has a quantitative contrast. (iii) The best possible resolution is not solely defined by the NA of the reporter but by the maximum diffraction angle which is recorded by the detector. This is because in addition to the magnified near field, the conventional CDI signal is also recorded. The CDI signal may dominate at high angles for strongly scattering samples and MZPs of moderate resolution. (iv) The full signal of diffracted and nondiffracted photons as well as positive and negative diffraction orders can be used for phase retrieval, increasing photon efficiency and reducing the sample dose. (v) Aberrations of the MZP do not result in distortions of the reconstructed sample structure. Note that unlike x-ray microscopes using point-to-point imaging optics, the depth of field limit (of the sample) can be extended using multislice approaches similar to ptychography [41]. At the same time, we do not want to conceal that TXMs are better suited for low coherence and have demonstrated impressive imaging results in material science with resolutions down to 10 nm in absorption contrast [4].

Finally, a discussion of RBI compared to inline holography. Inline holography is a phase-sensitive imaging scheme that can cover large specimens and is due to its dose efficiency well suited for imaging biological tissues [19]. The resolution of holographic imaging is limited by the source size of the illumination, which can be challenging with respect to wave front artifacts [42,43]. Novel approaches which can achieve superresolution with respect to the source spot NA depend on the application of waveguide filtering [5]. Since a focused beam needs to be coupled into the waveguide, typically with channel dimensions below 100 nm, this scheme is not easily implemented at FELs where high focus intensities could damage the waveguide. Contrarily, the MZP optic of the RBI scheme is illuminated over areas of several micrometers, resulting in lower peak intensities.

In conclusion, we have presented a novel coherent diffractive imaging approach using a reporter structure and achieving a sub-10-nm (half-period) resolution with quantitative phase contrast. The scheme is based on the coherent full-field illumination of a sample, a MZP positioned in the near field, and the recording of the diffraction pattern in the far field. We have shown that a single diffraction pattern recorded in this configuration encodes at least three complementary sample signals, the +first and −first MZP diffraction order and the CDI signal around the center beam. By treating all signals in a common reconstruction scheme, we have shown that the highest recorded diffraction angle can be exploited for high resolution, and the simultaneous presence of the positive and negative diffraction orders for a robust reconstruction which can be applied for isolated and nonisolated samples. By using the MZP transfer function directly within the iterative reconstruction scheme, we overcome limitations imposed by aberrations or distortions of the reporter structure. Further, sample to MZP distance allows for an additional control parameter for contrast variation. Finally, we stress that RBI does not require the use of point-to-point imaging optics as a reporter. Instead, the diffractive reporter structure could be favorably designed and generalized to a wider class of diffractive optics suitable to report the wave field.

We thank Christian Eberl for the fabrication and Mike Kanbach for the mounting of the MZP. Further, we thank Jesper Wallentin and Lert Chayanun for providing the NWs and the discussions on rotational twinning, as well as Lukas Hrachowina and Magnus Borgström for the NW fabrication. We also would like to thank Michael Sprung, Fabian Westermeier, and Anna-Lena Robisch for assistance during the beamtime. Finally, we thank Jan Goeman for discussion and advice in computing. Financial support by German Federal Ministry of Education and Research (BMBF) through Grant No. 05K19MG2 and the Deutsche Forschungsgemeinschaft (DFG) Grants No. SFB 755 and No. SFB 1456 was gratefully acknowledged.

*jakob.soltau@uni-goettingen.de
†tsaldit@gwdg.de

[1] H. Öztürk, H. Yan, Y. He, M. Ge, Z. Dong, M. Lin, E. Nazaretski, I. K. Robinson, Y. S. Chu, and X. Huang, Multi-slice ptychography with large numerical aperture multilayer Laue lenses, Optica **5**, 601 (2018).

[2] P. Villanueva-Perez, B. Pedrini, R. Mokso, P. Vagovic, V. A. Guzenko, S. J. Leake, P. R. Willmott, P. Oberta, C. David, H. N. Chapman, and M. Stampanoni, Hard x-ray multiprojection imaging for single-shot approaches, Optica **5**, 1521 (2018).

[3] M. Holler, M. Odstrcil, M. Guizar-Sicairos, M. Lebugle, E. Müller, S. Finizio, G. Tinti, C. David, J. Zusman, W. Unglaub *et al.*, Three-dimensional imaging of integrated circuits with macro- to nanoscale zoom, National electronics review **2**, 464 (2019).

[4] V. De Andrade, V. Nikitin, M. Wojcik, A. Deriy, S. Bean, D. Shu, T. Mooney, K. Peterson, P. Kc, K. Li *et al.*, Fast x-ray nanotomography with sub-10 nm resolution as a powerful imaging tool for nanotechnology and energy storage applications, Adv. Mater. **33**, 2008653 (2021).

[5] J. Soltau, M. Vassholz, M. Osterhoff, and T. Salditt, In-line holography with hard x-rays at sub-15 nm resolution, Optica **8**, 818 (2021).

[6] J. Lim, Y. Li, D. H. Alsem, H. So, S. C. Lee, P. Bai, D. A. Cogswell, X. Liu, N. Jin, Y.-s. Yu *et al.*, Origin and hysteresis of lithium compositional spatiodynamics within battery primary particles, Science **353**, 566 (2016).

[7] K. Ayyer, P. L. Xavier, J. Bielecki, Z. Shen, B. J. Daurer, A. K. Samanta, S. Awel, R. Bean, A. Barty, M. Bergemann *et al.*, 3D diffractive imaging of nanoparticle ensembles using an x-ray laser, Optica **8**, 15 (2021).

[8] M. O. Wiedorn, D. Oberthür, R. Bean, R. Schubert, N. Werner, B. Abbey, M. Aepfelbacher, L. Adriano, A. Allahgholi, N. Al-Qudami *et al.*, Megahertz serial crystallography, Nat. Commun. **9**, 4025 (2018).

[9] M. Vassholz, H. P. Hoeppe, J. Hagemann, J. M. Rosselló, M. Osterhoff, R. Mettin, T. Kurz, A. Schropp, F. Seiboth, C. G. Schroer, M. Scholz *et al.*, Pump-probe x-ray holographic imaging of laser-induced cavitation bubbles with femtosecond FEL pulses, Nat. Commun. **12**, 3468 (2021).

[10] G. Schmahl, D. Rudolph, B. Niemann, and O. Christ, Zone-plate x-ray microscopy, Q. Rev. Biophys. **13**, 297 (1980).

[11] J. Miao, D. Sayre, and H. N. Chapman, Phase retrieval from the magnitude of the Fourier transforms of nonperiodic objects, J. Opt. Soc. Am. A **15**, 1662 (1998).

[12] J. Miao, T. Ishikawa, I. K. Robinson, and M. M. Murnane, Beyond crystallography: Diffractive imaging using coherent x-ray light sources, Science **348**, 530 (2015).

[13] J. M. Rodenburg, A. C. Hurst, A. G. Cullis, B. R. Dobson, F. Pfeiffer, O. Bunk, C. David, K. Jefimovs, and I. Johnson, Hard-X-Ray Lensless Imaging of Extended Objects, Phys. Rev. Lett. **98**, 034801 (2007).

[14] Y. Jiang, J. Deng, Y. Yao, J. A. Klug, S. Mashrafi, C. Roehrig, C. Preissner, F. S. Marin, Z. Cai, B. Lai, and S. Vogt, Achieving high spatial resolution in a large field-of-view using lensless x-ray imaging, Appl. Phys. Lett. **119**, 124101 (2021).

[15] R. Mokso, P. Cloetens, E. Maire, W. Ludwig, and J.-Y. Buffière, Nanoscale zoom tomography with hard x rays using Kirkpatrick-Baez optics, Appl. Phys. Lett. **90**, 144104 (2007).

[16] M. Bartels, M. Krenkel, J. Haber, R. N. Wilke, and T. Salditt, X-Ray Holographic Imaging of Hydrated Biological Cells in Solution, Phys. Rev. Lett. **114**, 048103 (2015).

[17] J. Cesar da Silva, A. Pacureanu, Y. Yang, S. Bohic, C. Morawe, R. Barrett, and P. Cloetens, Efficient concentration of high-energy x-rays for diffraction-limited imaging resolution, Optica **4**, 492 (2017).

[18] A. Khimchenko, H. Deyhle, G. Schulz, G. Schweighauser, J. Hench, N. Chicherova, C. Bikis, S. E. Hieber, and B. Müller, Extending two-dimensional histology into the third dimension through conventional micro computed tomography, NeuroImage **139**, 26 (2016).

[19] M. Töpperwien, F. van der Meer, C. Stadelmann, and T. Salditt, Three-dimensional virtual histology of human cerebellum by x-ray phase-contrast tomography, Proc. Natl. Acad. Sci. U.S.A. **115**, 6940 (2018).

[20] F. Döring, A. L. Robisch, C. Eberl, M. Osterhoff, A. Ruhlandt, T. Liese, F. Schlenkrich, S. Hoffmann, M. Bartels, T. Salditt, and H. U. Krebs, Sub-5 nm hard x-ray point focusing by a combined Kirkpatrick-Baez mirror and multilayer zone plate, Opt. Express **21**, 19311 (2013).

[21] S. Bajt, M. Prasciolu, H. Fleckenstein, M. Domarackÿ, H. N. Chapman, A. J. Morgan, O. Yefanov, M. Messerschmidt, Y. Du, K. T. Murray *et al.*, X-ray focusing with efficient high-NA multilayer Laue lenses, Light Sci. Appl. **7**, 17162 (2018).

[22] J. Soltau, L. Chayanun, M. Lyubomirskiy, J. Wallentin, and M. Osterhoff, Off-axis multilayer zone plate with 16 nm $\times$ 28 nm focus for high-resolution x-ray beam induced current imaging, J. Synchrotron Radiat. **28**, 1573 (2021).

[23] T. Salditt, M. Osterhoff, M. Krenkel, R. N. Wilke, M. Priebe, M. Bartels, S. Kalbfleisch, and M. Sprung, Compound focusing mirror and x-ray waveguide optics for coherent imaging and nano-diffraction, J. Synchrotron Radiat. **22**, 867 (2015).

[24] J. Soltau, L. M. Lohse, M. Osterhoff, and T. Salditt, Finite-difference propagation for the simulation of x-ray multilayer optics, Opt. Express **29**, 41932 (2021).

[25] C. Eberl, F. Döring, T. Liese, F. Schlenkrich, B. Roos, M. Hahn, T. Hoinkes, A. Rauschenbeutel, M. Osterhoff, T. Salditt, and H.-U. Krebs, Fabrication of laser deposited high-quality multilayer zone plates for hard x-ray nanofocusing, Appl. Surf. Sci. **307**, 638 (2014).

[26] H. M. Quiney, A. G. Peele, Z. Cai, D. Paterson, and K. A. Nugent, Diffractive imaging of highly focused x-ray fields, Nat. Phys. **2**, 101 (2006).

[27] B. Abbey, K. A. Nugent, G. J. Williams, J. N. Clark, A. G. Peele, M. A. Pfeifer, M. de Jonge, and I. McNulty, Keyhole coherent diffractive imaging, Nat. Phys. **4**, 394 (2008).

[28] A. M. Maidenand and J. M. Rodenburg, An improved ptychographical phase retrieval algorithm for diffractive imaging, Ultramicroscopy **109**, 1256 (2009).

[29] T. Salditt, A. Egner, and D. R. Luke, *Nanoscale Photonic Imaging* (Springer Nature, New York, 2020).

[30] S. P. Krüger, H. Neubauer, M. Bartels, S. Kalbfleisch, K. Giewekemeyer, P. J. Wilbrandt, M. Sprung, and T. Salditt, Sub-10 nm beam confinement by x-ray waveguides: Design, fabrication and characterization of optical properties, J. Synchrotron Radiat. **19**, 227 (2012).

[31] D. R. Luke, Relaxed averaged alternating reflections for diffraction imaging, Inverse Probl. **21**, 37 (2004).

[32] J. Wallentin, M. Ek, L. R. Wallenberg, L. Samuelson, K. Deppert, and M. T. Borgström, Changes in contact angle of seed particle correlated with increased zincblende formation in doped InP nanowires, Nano Lett. **10**, 4807 (2010).

[33] F. Zhang, B. Chen, G. R. Morrison, J. Vila-Comamala, M. Guizar-Sicairos, and I. K. Robinson, Phase retrieval by coherent modulation imaging, Nat. Commun. **7**, 1 (2016).

[34] A. Robisch, K. Kröger, A. Rack, and T. Salditt, Near-field ptychography using lateral and longitudinal shifts, New J. Phys. **17**, 073033 (2015).

[35] See Supplemental Material at http://link.aps.org/supplemental/10.1103/PhysRevLett.128.223901 which includes Refs. [23,25,36–40].

[36] A. Zozulya, S. Bondarenko, A. Schavkan, F. Westermeier, G. Grübel, and M. Sprung, Microfocusing transfocator for 1D and 2D compound refractive lenses, Opt. Express **20**, 18967 (2012).

[37] M. Osterhoff, C. Eberl, J. Soltau, and H.-U. Krebs, Preparing for hard x-ray microscopy with multilayer zone plates, J. Phys. Conf. Ser. **849**, 012049 (2017).

[38] S. Marchesini, H. He, H. N. Chapman, S. P. Hau-Riege, A. Noy, M. R. Howells, U. Weierstall, and J. C. H. Spence, X-ray image reconstruction from a diffraction pattern alone, Phys. Rev. B **68**, 140101(R) (2003).

[39] P. Cloetens, W. Ludwig, J. Baruchel, D. Van Dyck, J. Van Landuyt, J. P. Guigay, and M. Schlenker, Holotomography: Quantitative phase tomography with micrometer resolution using hard synchrotron radiation x rays, Appl. Phys. Lett. **75**, 2912 (1999).

[40] H. N. Chapmanand and S. Bajt, A ray-trace analysis of x-ray multilayer Laue lenses for nanometer focusing, J. Opt. **22**, 115610 (2020).

[41] E. H. R. Tsai, I. Usov, A. Diaz, A. Menzel, and M. Guizar-Sicairos, X-ray ptychography with extended depth of field, Opt. Express **24**, 29089 (2016).

[42] J. Hagemann, A.-L. Robisch, M. Osterhoff, and T. Salditt, Probe reconstruction for holographic x-ray imaging, J. Synchrotron Radiat. **24**, 498 (2017).

[43] A. J. Morgan *et al.*, Ptychographic x-ray speckle tracking with multi-layer Laue lens systems, J. Appl. Crystallogr. **53**, 927 (2020).